Modeling and Optimization of Biomimetic Magnetic Cilia for Multifunctional Tactile Sensor

Kan Liu[a,b], Huangzhe Dai[a,b], Kaicheng Luo[c], Zuyao Zhang[d], Chengfeng Pan[a,b], Chengqian Zhang[a,b*],Peng Zhao[a,b]

[a] *The State Key Laboratory of Fluid Power and Mechatronic Systems, College of Mechanical Engineering, Zhejiang University, Hangzhou 310027, China*

[b] *The Key Laboratory of 3D Printing Process and Equipment of Zhejiang Province, College of Mechanical Engineering, Zhejiang University, Hangzhou 310027, China*

[c] *School of Mathematical Sciences, Zhejiang University, 310027, Hangzhou, China*

[d] *School of Physics, Zhejiang University, 310027, Hangzhou, China*

[*] *Corresponding Author Email: zhangcq@zju.edu.cn*

Abstract:

Tactile sensing is an essential component of robotic perception, enabling robots to acquire detailed information about contact interactions with the environment. Among various sensing strategies, biomimetic cilia-inspired magnetic tactile sensors have emerged as promising candidates due to their high sensitivity, flexible structure, and remote readout capabilities. These sensors emulate the function of natural cilia found in organisms such as fish and insects, which rely on slender hair-like structures to detect fluid flow, vibration, and surface features. However, the design and optimization of artificial magnetic cilia have largely relied on empirical calibration and qualitative analysis, limiting scalability and performance predictability. In this study, we propose a quantitative theoretical model that captures the coupled mechanical and magnetic behavior of cilia-based tactile sensors. The model represents the cilium as a two-segment beam composed of non-magnetic base and magnetic tip, and incorporates both concentrated and distributed loading conditions to simulate real-world interactions. The model shows strong agreement with both finite element simulations and experimental results ($R^2 > 0.99$), confirming its accuracy. Design parameter studies reveal how material stiffness, aspect ratio, and magnetic segment proportion influence sensitivity and range. The sensor achieves multidirectional flow detection (0∼0.5 m/s with <10° angular error) and surface texture discrimination, providing a predictive foundation for advanced tactile sensor development in robotic manipulation and fluidic environments.

Keywords:

magnetic cilia, tactile sensor, biomimetic sensing, flow field perception, surface characterization, theoretical modeling

1 Introduction

With the rapid development of robotics, higher demands have been placed on the environmental perception capabilities of robotic systems. Among various perception modalities, tactile sensing plays a critical role in emulating the human skin's ability to respond sensitively to external contact stimuli. Tactile sensors enable robots to acquire a wide range of contact-related information, including pressure [1,2], shear force [3], vibration [4], surface roughness [5], liquid flow [6], and even airflow [7]. These sensors have been widely deployed in various cutting-edge applications, such as precision manipulation and grasping control in robotic arms [8,9], flow field velocity and vortex detection [10], development of biomimetic electronic skin [11,12], tactile feedback in highly sensitive intelligent prosthetics [13,14], and haptic modules in augmented reality and human–machine interaction systems [15]. To meet the diverse requirements of these applications, tactile sensors based on various working principles have been developed, including strain sensors utilizing resistive changes [4,16], flexible capacitive tactile

arrays [17,18], and piezoelectric-based sensors capable of both nanomaterial-based therapy and virus detection [19]. Among them, tactile sensors based on magnetic sensing mechanisms have emerged as a promising technique due to their high sensitivity, flexible structural design, ease of integration, and capability for remote readout.

In various organisms in nature, highly sensitive cilia-like structures are extensively utilized for environmental perception [20,21]. For instance, fish rely on lateral line systems to perceive flow direction and strength [8], while cockroaches utilize antennae to perform wall-following navigation [5]; even the microstructures on lotus leaves demonstrate excellent environmental sensitivity [22]. Inspired by these natural ciliary structures, researchers have integrated cilia into tactile sensor designs to enhance resolution and responsiveness to subtle tactile stimuli [3,5,23]. With the rapid advancement of magnetic sensing technologies, it has become feasible to construct artificial magnetic cilia with magnetic responsiveness. Deformation of the cilium induced by external forces or fluid flows leads to variations in the magnetic field, which can be detected to facilitate highly sensitive responses to complex tactile stimuli [4,24]. However, current research on such magnetic tactile sensors predominantly relies on extensive experimental calibration and qualitative phenomenological analyses. There remains a lack of quantitative theoretical models to guide the design and fabrication of magnetic tactile cilia. Additionally, existing simulation tools are inadequate for accurately modeling the behavior of deformable magnetic structures. This empirical approach limits the predictability and design optimization of magnetic cilia-based tactile sensors.

To address the modeling challenges associated with soft magnetic cilia sensors, we propose a comprehensive theoretical model grounded in solid mechanics and magnetic dipole approximation. This model captures the coupling between mechanical deformation and magnetic field variation under different external stimuli. Specifically, it differentiates between two distinct loading scenarios: concentrated forces (e.g., localized contact at the cilium tip) and distributed forces (e.g., fluid flow interactions in idealized scenarios). By analyzing the bending behavior of the composite magnetic rod under these loading conditions, the model quantitatively predicts both deflection profiles and resulting magnetic field perturbations. Under this configuration, the significant stiffness contrast leads to deformation predominantly occurring in the non-magnetic region, which aligns well with both finite element simulations and experimental measurements, thereby supporting the validity of the bending model. The magnetic segment is treated as a magnetic dipole (or a series of dipoles), and field computation is performed numerically at multiple observation points due to the lack of closed-form expressions. Comparative analysis between single-dipole and multi-dipole approaches confirms the validity of the simplified single-dipole model, which balances computational efficiency (O(n) complexity) with high accuracy ($R^2 > 0.99$ for both B_x and B_y). Building upon this validated model, we systematically investigate how key design parameters—such as the Young's moduli of the non-magnetic and magnetic segments, the geometric aspect ratio (L_0/d), and the magnetic segment proportion (L_2/L_0)—affect sensing range and resolution. This enables scenario-driven optimization of sensor design without the need for extensive empirical iteration. As a result, we successfully tailor the magnetic cilia sensor for specific functionalities, including multidirectional steady-state flow detection, surface topography sensing, and surface material differentiation.

2 Methods and theory

2.1 Sample preparation

The sensing element of a sensor may consist of either an array of magnetic cilia or an individual cilium structure. For clarity, the following discussion focuses on a single cilium configuration. A flexible magnetic cilium typically consists of two distinct segments: a non-magnetic lower section and a magnetic upper section. The non-magnetic segment is usually fabricated from compliant materials such as PDMS (Sylgard 184 Silicone Elastomer, Dow Corning Corporation) or silicone rubber (Ecoflex 0030, Smooth-On). These materials require curing with a cross-linking agent under controlled temperature conditions, where both curing duration and temperature significantly influence the mechanical properties of the final product. The magnetic segment is typically a composite material

formed by embedding magnetic particles within a flexible matrix prior to curing. The Young's modulus of this composite exhibits a positive correlation with the mass fraction of the incorporated magnetic particles. To ensure uniform magnetization characteristics, we employed high-quality NdFeB particles (5 μm diameter) as the magnetic filler[25]. The magnetic properties of these particles are detailed in Table 1. As a class of hard magnetic materials, these NdFeB particles demonstrate superior magnetic performance, including high remanent flux density, substantial coercivity, and exceptional responsiveness to applied magnetic fields.

Table 1

The magnetic performance of the NdFeB particles used in the experiment was characterized by three key parameters: remanent flux density B_r, energy density W, and intrinsic coercivity H_{ci}.

	Specified	Reference
B_r	$838 - 878\ mT$	$8.38 - 8.78\ KG$
W	$105 - 117\ kJ/m^3$	$13.2 - 14.7\ MGOe$
H_{ci}	$710 - 780\ kA/m$	$8.9 - 9.8\ kOe$

Previous studies have documented two predominant fabrication methods for flexible magnetic cilium. The first approach employs a mold-based technique, where a rigid mold is initially perforated using fused deposition modeling (FDM), laser micromachining, or photolithographic etching[26]. Subsequently, a mixture of flexible polymer matrix and magnetic particles is introduced into the mold cavities, followed by curing and magnetization processes to produce demoldable cilia. The second method, known as metal tube pressing (MTP)[7], involves casting the magnetic composite mixture onto a planar substrate to form a bilayer structure. After curing and magnetization, hollow metal tubes are vertically pressed through the sample, enabling extraction of the solidified magnetic cilia through mechanical withdrawal from the tubes.

These two fabrication methods exhibit distinct advantages and limitations, making them suitable for different applications. The mold-based method produces magnetic cilia with high dimensional accuracy determined by the mold precision, typically yielding uniform cylindrical structures with excellent consistency and experimental reproducibility. However, this method faces challenges in demolding high-aspect-ratio cilia and may encounter incomplete mold filling when using high magnetic particle concentrations, often resulting in bubble formation. To address these limitations, we implemented two key modifications: (1) as illustrated in Fig. 1(a), a split-mold design that reduces the effective demolding length by separating the magnetic section mold into two components, enabling fabrication of cilia with larger aspect ratios; and (2) a vacuum-assisted process where the filled mold is placed in a vacuum chamber to create negative pressure, significantly reducing bubble formation through enhanced material flow under atmospheric pressure. In contrast, the metal tube pressing (MTP) method demonstrates unique advantages for fabricating slender cilia. Its large casting area combined with vacuum treatment effectively eliminates bubble formation, producing dense cilia structures. Nevertheless, MTP requires stringent conditions: the metal tubes must have sharp edges and perfect vertical alignment to facilitate cilia extraction, and any angular deviation during insertion compromises results. Additionally, MTP-produced cilia typically exhibit diameter variations and poor consistency, while the process itself consumes substantial material, resulting in higher costs.

The magnetic cilia were fabricated using a mold-based method to ensure high dimensional accuracy, which is critical for validating the theoretical model. To minimize experimental errors caused by the limited resolution of the force sensor, thicker cilia were fabricated to amplify the measurable force. The mold was produced via fused deposition modeling (FDM), with a split-mold design to separately form the non-magnetic and magnetic segments. First, PDMS (Sylgard 184 Silicone Elastomer, Dow Corning Corporation) and curing agent were mixed in a 10:1 weight ratio in a plastic cup and degassed in a centrifuge for 30 seconds to remove air bubbles. The mixture was then poured into the lower mold and placed in a vacuum chamber to ensure complete mold infiltration. The assembly

was cured at 80 °C for 8 hours to solidify the pure PDMS segment, after which excess material was trimmed. The upper mold, consisting of two detachable parts to facilitate demolding, was then aligned and secured. Next, a second PDMS mixture with NdFeB particles (5 μm average diameter) was prepared at a controlled mass ratio (adjustable based on desired magnetic properties). After thorough mixing and degassing, the composite was poured into the upper mold, vacuum-treated, and thermally cured under identical conditions. As shown in Fig. 1(b), the solidified cilia were magnetized in a vertical pulsed magnetic field and demolded. As shown in Fig. 1(c), for sensor assembly, the cilium was vertically mounted on an 18×18 mm coverslip using fast-curing adhesive. As illustrated in Fig. 1(d), the MLX90393 sensor was positioned in a 3D-printed holder, and a 24×24 mm coverslip was adhered to the housing to ensure a flat surface. The smaller coverslip was then aligned on the larger one, with fine adjustments made until the sensor outputs (B_x, B_y) approached zero, followed by adhesive fixation to complete the sensor prototype.

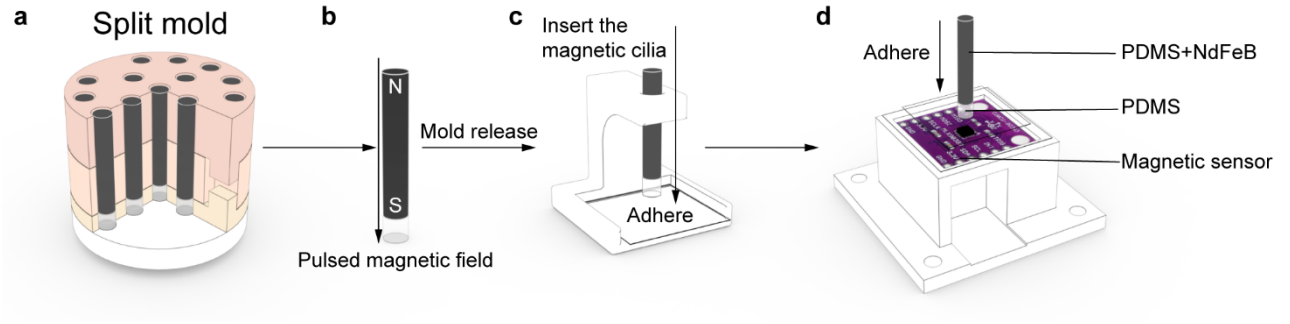

Fig. 1. Fabrication process of the magnetic cilia-based sensor. (a) Split-mold design to facilitate demolding of high-aspect-ratio magnetic segments. (b) Demolded magnetic cilia after curing and magnetize. (c) Bonding the cilia to an 18×18 mm coverslip using epoxy. (d) Final sensor assembly with alignment on a 24×24 mm coverslip.

2.2 Theoretical model

Based on principles of solid mechanics and magnetostatics, we developed a theoretical model to characterize spatial magnetic field variations generated by the bending deformation of magnetic cilia, as shown in Fig. 2(a). The analysis considers two mechanical loading scenarios: (1) concentrated point forces and (2) distributed forces, both of which induce curvature in the magnetized segment. Due to the nonlinear geometric deformation, conventional finite-element simulation methods become computationally intractable. To overcome this limitation, we discretized the bent magnetic segment into sequentially aligned magnetic dipoles. The resultant magnetic field was then derived through spatial integration of these dipole contributions, accounting for both orientation and position changes induced by cilia deflection.

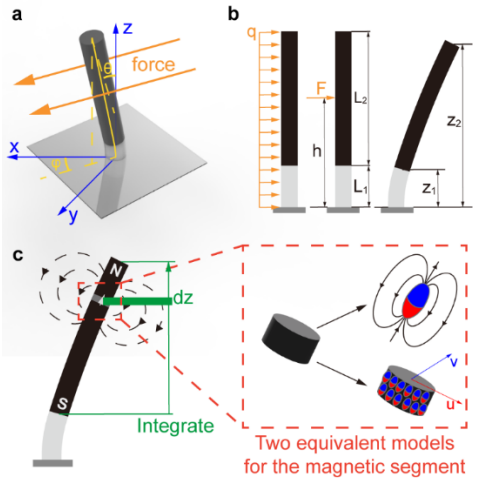

Fig. 2. (a) Schematic of force-induced cilia bending with coordinate system definition (b) Key parameters for bending calculation (c) Two approaches for magnetic segment discretization

2.2.1 Solid Mechanics: Bending Modeling

The concentrated force scenario represents a simplified loading condition where external forces are assumed to act at a single point along the cilium (e.g., contact forces from manual manipulation or object interaction). For analytical tractability, we consider horizontal forces parallel to the base plane, with the contact point maintaining constant height during deflection. The cilium is modeled as a cantilever beam with segmented material properties.

As shown in Fig. 2(b), for concentrated force, the cilium can be divided into three mechanically distinct segments: (i) the non-magnetic segment ($0 < z < z_1$), (ii) the lower magnetic segment between the non-magnetic tip and force application point ($z_1 < z < h$), and (iii) the upper magnetic segment from the force point to the cilium tip ($h < z < z_2$). Solving the equations (see SUPPLEMENTAL INFORMATION for details) yields the simplified form:

$$\frac{\partial w(F,z)}{\partial \mathrm{z}} = \begin{cases} \pm \dfrac{Fz(z-2h)}{\sqrt{4(E_1I)^2 - F^2z^2(z-2h)^2}}, 0 < z < z_1 \\ \pm \dfrac{1}{\Gamma_1}, z_1 < z < h \\ \pm \dfrac{1}{\Gamma_1}\Big|_{z=h}, h < z < z_2 \end{cases} \tag{1}$$

z_1 and z_2 are determined by the following system of equations:

$$\begin{cases} \displaystyle\int_0^{z_1} \sqrt{1 + \left(\frac{\partial w(F,z)}{\partial \mathrm{z}}\right)^2}\, \mathrm{d}z = L_1 \\ \displaystyle\int_{z_1}^{h} \sqrt{1 + \frac{1}{\Gamma_1{}^2}}\, dz + \int_h^{z_2} \sqrt{1 + \tan^2\theta_2}\, dz = L_2 \end{cases} \tag{2}$$

The fundamental distinction between distributed and concentrated loads lies in their respective moment formulations. For distributed loading conditions,

$$\frac{\partial w(q,z)}{\partial \mathrm{z}} = \begin{cases} \pm \dfrac{qz(-3z_2^2 + 3z_2z - z^2)}{\sqrt{36(E_1I)^2 - q^2z^2(-3z_2^2 + 3z_2z - z^2)^2}}, 0 < z < z_1 \\ \pm \dfrac{1}{\Gamma_2}, z_1 < z < z_2 \end{cases} \tag{3}$$

z_1 and z_2 are determined by the following system of equations:

$$\begin{cases} \displaystyle\int_0^{z_1} \sqrt{1 + \left(\frac{\partial w(q,z)}{\partial \mathrm{z}}\right)^2}\, \mathrm{d}z = L_1 \\ \displaystyle\int_{z_1}^{z_2} \sqrt{1 + \left(\frac{\partial w(q,z)}{\partial \mathrm{z}}\right)^2}\, \mathrm{d}z = L_2 \end{cases} \tag{4}$$

Where F represents the concentrated force load, q denotes the distributed load intensity, L_1 corresponds to the initial axial length of the non-magnetic flexible segment, h indicates the axial distance between the concentrated load application point and the fixed end, L_2 signifies the initial axial length of the magnetic flexible segment, E_1 and E_2 represent Young's moduli of the non-magnetic and magnetic materials respectively, I is the second moment of area, calculated as $I = \pi d^4/64$, where d is the diameter of the cilia, θ_1 denotes the rotation angle at the terminus of the non-magnetic segment, θ_2 is the rotation angle at the concentrated load application point, as shown in Fig. 2(b), the parameter Γ_1 and Γ_2 are defined in SUPPLEMENTAL INFORMATION.

Due to the lack of closed-form solutions, all integrals are evaluated numerically using MATLAB's adaptive quadrature methods. The numerical outcomes are detailed in the Results and Discussion section.

2.2.2 Magnetostatics: Bent Cilium Field Modeling

The initial magnetization orientation was axial, but bending induces heterogeneous stress distributions and

deformation states along the cilium. To model this, we discretize the deformed cilium into sequentially aligned magnetic dipoles, effectively representing cross-sectional slices perpendicular to the local axial direction. The total magnetic field is obtained through linear superposition of contributions from all slices. For an infinitesimal segment dz at height z, treated as a point dipole, the magnetic field distribution follows[27]:

$$d\boldsymbol{B} = \frac{\mu_0}{4\pi}\frac{1}{a^3}[3(\boldsymbol{m}\cdot\hat{\boldsymbol{a}})\hat{\boldsymbol{a}} - \boldsymbol{m}] = \frac{\mu_0}{4\pi}\frac{1}{a^5}[3(\boldsymbol{m}\cdot\boldsymbol{a})\boldsymbol{a} - a^2\boldsymbol{m}] \tag{5}$$

where $\boldsymbol{m}$ stands for magnetic moment vector, $\hat{\boldsymbol{a}}$ is the unit vector from dipole center to observation point, $\boldsymbol{a}$ is the vector from dipole center to observation point, $a = |\boldsymbol{a}|$ is the distance to observation point, μ_0 is the vacuum permeability ($4\pi \times 10^{-7} H/m$).

Resolve $d\boldsymbol{B}$ into Cartesian components (see SUPPLEMENTAL INFORMATION for details):

$$\begin{cases} dB_x = \dfrac{\mu_0}{4}\dfrac{R^2 M}{a^5}[3\Lambda_1(x_0 - w(z)\cos\varphi) - a^2\sin\theta\cos\varphi]\ \dfrac{dz}{\cos\theta} \\ dB_y = \dfrac{\mu_0}{4}\dfrac{R^2 M}{a^5\cos\theta}[3\Lambda_1(y_0 - w(z)\sin\varphi) - a^2\sin\theta\sin\varphi]\ \dfrac{dz}{\cos\theta} \\ dB_z = \dfrac{\mu_0}{4}\dfrac{R^2 M}{a^5\cos\theta}[3\Lambda_1(z_0 - z) - a^2\cos\theta]\dfrac{dz}{\cos\theta} \end{cases} \tag{6}$$

By integrating the above equation, the magnetic field components are given as follows:

$$B_i = \int_{z_1}^{z_2} dB_i\ (i = x, y, z) \tag{7}$$

Since the deflection $w(z)$ lacks an explicit analytical expression, we employ numerical integration by discretizing the interval $[0, z_2]$ into N segments of uniform length $dz = z_2/N$. The magnetic field contribution from each segment at the observation point is computed and summed to obtain the total theoretical field. Consistent with fundamental calculus principles, the solution's accuracy depends on the discretization resolution, asymptotically approaching the true value as $N \to \infty$.

While the preceding analysis treats each magnetic segment as a single equivalent dipole, higher-fidelity modeling can be achieved by discretizing the segment into multiple dipole elements. As illustrated in Fig. 2(c), to implement this approach, we introduce a local curvilinear coordinate system (u, v), aligned with the deformed cilium's principal axes. To facilitate integration, we implement a polar coordinate transformation ($u = r\cos\phi, v = r\sin\phi$), ultimately resolving $d\boldsymbol{B}$ into Cartesian components (see SUPPLEMENTAL INFORMATION for details):

$$\begin{cases} dB_x = \dfrac{\mu_0}{4\pi}\dfrac{Mr}{a^5\cos\theta}[3\Lambda_2 a_x - a^2\sin\theta\cos\varphi]\dfrac{dz}{\cos\theta}drd\phi \\ dB_y = \dfrac{\mu_0}{4\pi}\dfrac{Mr}{a^5\cos\theta}\left[3\Lambda_2 a_y - a^2\sin\theta\sin\varphi\right]\ \dfrac{dz}{\cos\theta}drd\phi \\ dB_z = \dfrac{\mu_0}{4\pi}\dfrac{Mr}{a^5\cos\theta}[3\Lambda_2 a_z - a^2\cos\theta]\dfrac{dz}{\cos\theta}drd\phi \end{cases} \tag{8}$$

By integrating the above equation, the magnetic field components are given as follows:

$$B_i = \int_{z=z_1}^{z_2}\int_{r=0}^{R}\int_{\phi=0}^{2\pi} dB_i\ (i = x, y, z) \tag{9}$$

The complete numerical results are presented in the Results and Discussion section.

3 Results and discussion

3.1 Design and commissioning of the test bench

Concentrated loading conditions were employed for experimental convenience in model validation, with suitable parameters selected to verify theoretical predictions. The MLX90393 Hall-effect sensor was selected for

precise spatial magnetic field measurements, with its SCL, SDA, 3.3V, and GND pins connected to the microcontroller's A5, A4, 3.3V, and GND terminals respectively. Successful connection was confirmed by illumination of the microcontroller's TX indicator light, after which serial communication was established using aircraft-grade debugging software to display and record triaxial data on a PC.

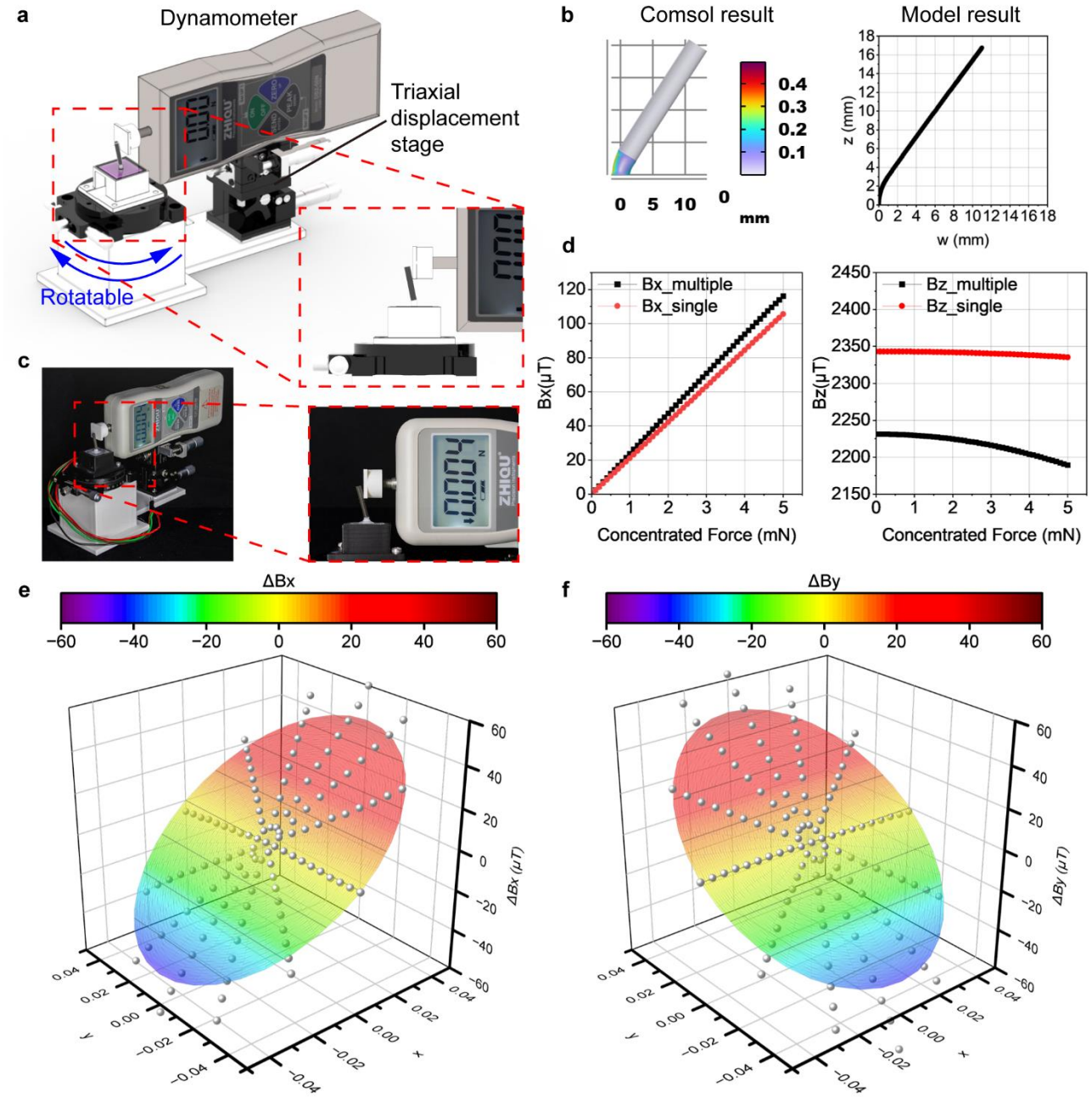

Fig. 3. (a) Schematic diagram of the concentrated-force magnetic cilium bending test platform; (b) Comparison between COMSOL simulation results and theoretical model results for cilium deformation; (c) Physical implementation of the concentrated-force test platform; (d) Computational results comparison for two magnetic cilium models; (e) Correlation between theoretical magnetic field predictions and experimental measurements.

As illustrated in Fig. 3(a)(c), The experimental setup incorporated a three-axis precision positioning system (HENGYANG HRS60-L, HXY40-LM, and HLZ-40 stages; Guangzhou Hengyang Electronic Technology Co., Ltd., Guangdong, China) and a DS2-5 digital force gauge (Dongguan ZhiQu Precision Instruments Co., Ltd., Guangdong, China). To minimize magnetic interference, the original force gauge tip was replaced with a custom PLA 3D-printed probe secured via interference-fit threading to ensure perpendicular force application. The sensor assembly was

mounted on the HRS60-L rotation stage while the force gauge was fixed to the HXY40-LM and HLZ-40 stages, with their relative positions maintained by 3D-printed fixture. Prior to final assembly of the magnetic cilium, ambient geomagnetic field measurements were taken at 30° intervals and subsequently subtracted from experimental data. Following coverslip alignment and adhesive curing, measurements were conducted by advancing the force gauge in controlled increments while simultaneously recording magnetic field data, applied force, and stage displacement. Angular dependence was characterized by rotating the HRS60-L stage between measurement sequences, with directional geomagnetic compensation applied in software, ultimately completing full angular characterization.

3.2 Deformation Computation and Validation

The computational results derived from the theoretical model were visualized and compared with both finite element simulations and experimental measurements. As shown in Fig. 3(b), the calculated results demonstrate good agreement with both the simulated field distributions and experimental observations. This correspondence validates the theoretical model, particularly regarding the mechanical deformation analysis. The Young's modulus contrast between segments - where the non-magnetic silicone segment (E $\approx$ 0.1 MPa) exhibits approximately two orders of magnitude lower stiffness than the magnetic PDMS composite (E $\approx$ 3 MPa) - results in predominant deformation occurring in the non-magnetic region. This mechanical behavior, which aligns precisely with the model's predictions, confirms the validity of the solid mechanics bending modeling in our theoretical approach.

3.3 Magnetic Field Computation and Validation

The magnetic field integrals in this study lack closed-form solutions, necessitating numerical computation. We implemented two distinct approaches for modeling the magnetic segments: single-dipole model and multi-dipole model. As shown in Fig. 3(d), for comparative analysis, the horizontal field components (B_x and B_y) were combined into B_x, as they represent orthogonal projections of the same in-plane magnetic field. The multi-dipole model yielded marginally stronger horizontal fields ($\Delta B_x \approx 10.0\%$) but slightly weaker vertical fields (B_z reduced by $4.8 \sim 6.3\%$) compared to the single-dipole approach, and it exhibited greater sensitivity to force variations. Given the consistent trends and close numerical agreement (RRMSE: $B_x < 13\%$, $B_z < 6\%$), the single-dipole approximation was validated as an effective simplified model. This conclusion was further supported by computational efficiency considerations, as the multi-dipole model required 10^2-10^3 times longer execution times due to its $O(n^3)$ complexity versus the single-dipole's $O(n)$ scaling. Consequently, we adopted the single-dipole model for subsequent parametric optimization. As shown in Fig. 3(e), Experimental validation using the test platform confirmed strong correlation between measured B_x and B_y values and theoretical predictions (R^2: $B_x = 0.995, B_y = 0.993$).

3.4 Parameter Optimization Based on Theoretical Model

Following the validation of the theoretical model through experimental results, we proceed to investigate how key structural parameters influence the sensor's magnetic field response. This analysis provides valuable insights for tailoring sensor design to specific application requirements. Three principal parameters are examined: (1) the Young's moduli of the magnetic and non-magnetic segments, (2) the aspect ratio of the sensor (defined as the ratio of total length to diameter), and (3) the proportion of the magnetic segment relative to the total length. Each of these factors plays a distinct role in shaping the sensitivity and dynamic range of the sensor, as detailed below.

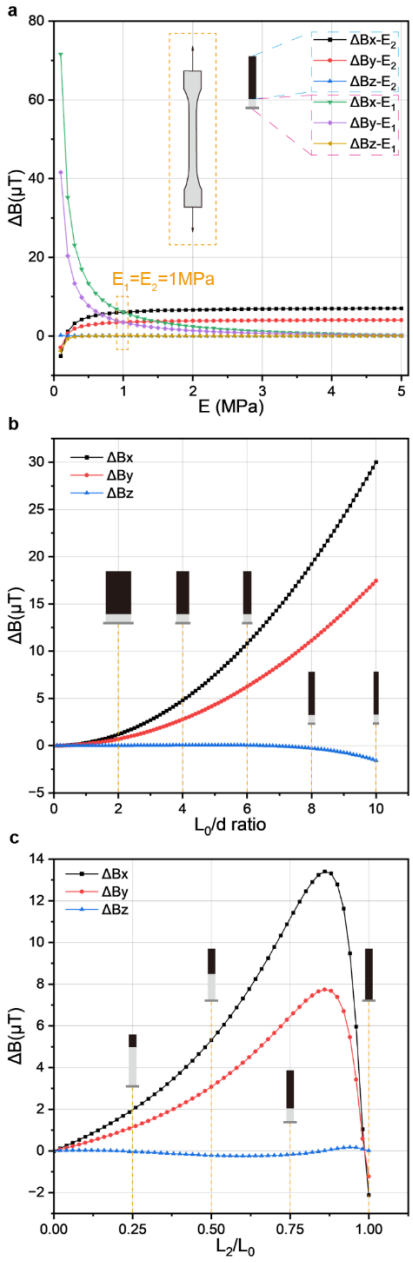

Fig. 4. Theoretical predictions of parametric influences on sensor performance. (a) Effect of Young's modulus of magnetic (E_2) and non-magnetic (E_1) segments (b) Sensitivity to aspect ratio variations (L_0/d, where L_0 is the total length, d is the diameter) (c) Performance dependence on magnetic segment proportion (L_2/L_0, where L_2 is the magnetic segment length)

3.4.1 Influence of Young's Modulus

Fig. 4(a) illustrates the three-axis magnetic field variation under applied force ($F = 0.001N, \varphi = 30°$) for the following fixed parameters: $L_1 = 3mm$, $L_2 = 17mm$, $h = 16mm$, $d = 3mm$, $M = 7.5 \times 10^4\, A/m$, $x_0 = -0.1mm$, $y_0 = 0.2mm$, $z_0 = -1.55mm$. For E_1 variation, $E_2 = 1$ MPa; for E_2 variation, $E_1 = 1$ MPa. We examine the role of mechanical stiffness in the two material segments. Specifically, we compare scenarios in which the Young's modulus of either the magnetic or non-magnetic segment is systematically varied, while the other is held constant. As shown in Fig. 4(a), increasing the stiffness of the non-magnetic segment results in a substantial reduction in the sensor's magnetic response under a fixed external force. This is because a stiffer non-magnetic region limits the extent of overall bending, thereby reducing the displacement of the magnetic segment and the resulting magnetic field perturbation.

Conversely, increasing the stiffness of the magnetic segment leads to an enhancement in the magnetic field variation, although this trend plateaus beyond a certain threshold. This occurs because a stiffer magnetic region maintains its shape more rigidly during deformation, amplifying the positional shift of the magnetic dipole relative to the sensing point. Taken together, these findings suggest that optimal performance is achieved by minimizing the modulus of the non-magnetic segment to maximize compliance, while selecting a stiffer magnetic material to enhance dipole displacement. This trade-off can be addressed either by selecting appropriate materials or by tuning the curing and fabrication conditions of the composite.

3.4.2 Influence of Aspect Ratio (L_0/d)

Fig. 4(b) shows the three-axis magnetic field variation with diameter d for fixed $L_1 = 3mm, L_2 = 17mm$, $E_1 = 0.5MPa, E_2 = 1MPa$ (other parameters as above). The results demonstrate that a higher aspect ratio amplifies field variation. We evaluate the impact of the sensor's aspect ratio, defined as the ratio of total length to diameter, on magnetic field sensitivity. In this case, we fix the total length and systematically decrease the diameter. The results, summarized in Fig. 4(b), indicate that a higher aspect ratio—achieved by reducing the diameter—significantly enhances the sensor's magnetic response.

Mechanistically, this effect arises because thinner structures exhibit greater curvature under the same applied load, resulting in more pronounced bending and, consequently, larger relative displacements of the magnetic segment. Although reducing the diameter also reduces the volume of magnetic material and the associated magnetic dipole moment, the increased deformation more than compensates for this reduction. As a result, the net magnetic field variation observed at the sensing point increases with higher aspect ratios. This trend underscores the importance of geometric scaling in optimizing sensor response, particularly in applications requiring high sensitivity within compact form factors.

3.4.3 Influence of Magnetic Segment Proportion (L_2/L_0)

Fig. 4(c) evaluates L_2 variation for $L_0 = 20\ mm$ and $d = 3\ mm$ (other parameters as above). The field variation peaks at $L_2/L_0 \approx 0.7–0.9$. We investigate the effect of varying the proportion of the magnetic segment relative to the total length of the sensor. As depicted in Fig. 4(c), the magnetic field variation exhibits a clear peak when the magnetic segment occupies approximately 70% to 90% of the total length. This non-monotonic behavior is governed by competing physical effects.

At low proportions, the amount of magnetic material is insufficient to generate significant magnetic perturbations, even though the structure remains highly compliant. As the magnetic segment length increases, the dipole moment grows, leading to stronger magnetic signals. However, when the magnetic segment approaches the full sensor length, two detrimental effects emerge. First, the overall mechanical flexibility is compromised due to the high stiffness of the magnetic material, limiting the extent of deformation under applied force. Second, when the magnetic segment is positioned too close to the observation point, small displacements translate into smaller changes in the detected field, diminishing the sensor's differential response.

Therefore, the optimal magnetic segment proportion strikes a balance between mechanical deformability and magnetic signal strength, typically favoring a dominant but not overwhelming contribution from the magnetic portion. These insights provide a basis for rational structural tuning to achieve desired trade-offs between sensitivity, robustness, and mechanical compatibility.

3.5 Perception of Multidirectional Steady-State Flow Field

One of the most important elements of hydrodynamic information is the velocity of the flow field. Therefore, the perception of flow velocity is one of the basic functions of hydrodynamic sensors.

Flow velocity is a fundamental hydrodynamic parameter, making its detection a core function of hydrodynamic sensors. In a steady-state flow field, the hydrodynamic force acting on an object is given by:

$$F_d = \frac{1}{2}\rho v^2 C_d A \tag{10}$$

For our experimental conditions, fluid density can be approximated as $\rho = 1 \times 10^3 kg/m^3$, flow velocity $v = 0 \sim 0.5m/s$, drag coefficient $C_d \approx 1$, effective area $A = d \times L_0$. Thus, the distributed force per unit length is

$$q = \frac{1}{2}\rho v^2 C_d d \tag{11}$$

For $d = 3mm$, the maximum load $q_{max} = 0.375N/m$. Given the small magnitude of this force, we selected silicone rubber (Ecoflex 0030, Smooth-On) for the non-magnetic segment to enhance sensitivity, which has low Young's modulus. The optimized sensor parameters were: $L_1 = 3mm,\ L_2 = 17mm,\ d = 3mm$.

As illustrated in Fig. 5(a), we constructed a closed-loop annular water tank using acrylic plates, capable of generating a stable annular flow field driven by four wave-maker pumps (MOW-22, Jebao Co., Ltd., Guangdong, China). These pumps and the experimental region were placed in two opposite linear sections of the channel. Toroidal flow deflectors were installed at the curved sections to mitigate vortex disturbances induced by the impeller blades of the pumps, thus preserving the stability of the flow field. The flow velocity ($= 0 \sim 0.5\ m/s$) could be regulated by adjusting the pump power. The dashed box in Fig. 5(a) marks the experimental area used for multidirectional steady-state flow field sensing. As shown in Fig. 5(b), the sensor was mounted at the base of a cylindrical, waterproof, 3D-printed housing, which could be immersed into the annular flow channel via a hole in the cover plate for flow velocity measurements. Consistent with the sensor setup above, a cover slip was placed atop the chip to ensure waterproofing. Additionally, the base was designed to be rotatable, allowing the cilia sensor to interact with flow fields from various directions within a unidirectional flow field generator.

Flow field experiments were conducted using the sensor, in which the fluid velocity was inferred from the detected variations in the magnetic field based on theoretical modeling. Theoretically, the magnetic field variation exhibits an approximately linear relationship with the force generated by the flow field. Since this force is proportional to the square of the flow velocity in low-speed regimes, a first-order linear function can be employed to fit the magnetic field variation against the squared velocity. A current meter (LS300A) was employed to obtain the average velocity in the region as a reference, against which the sensor's outputs were compared, as shown in Fig. 5(d). The results indicate that the sensor readings fluctuated around the reference velocity, due to unstable forces acting on the magnetic rod within the flow field. A minor offset could be observed between the time-averaged sensor readings and the reference velocity. This discrepancy can be attributed to the non-uniform velocity distribution in the flow field—velocity tends to be lower near the walls and higher in the center. Additionally, as shown in Fig. 5(c), the toroidal flow deflectors were not able to produce perfectly laminar flow; some vortex shedding and complex flow phenomena were present. As a result, modeling the flow-induced forces on the magnetic rod as a distributed load introduces an inherent approximation error.

One of the key advantages of our cilia sensor is its capability to simultaneously perceive both the direction and magnitude of a flow field using only a single 3D Hall sensor. By rotating the waterproof base, the sensor's orientation with respect to the flow direction could be altered, thereby enabling directional sensing within a unidirectional flow field. For each flow direction, five different velocity levels were tested to validate the sensor's performance in multidirectional flow velocity detection. Fig. 5(e) displays the sensor's response to varying angles of attack, with the horizontal and vertical axes representing the squared components of the flow velocity v_x^2 and v_y^2. The sensing points at identical velocities but different angles of attack form an approximate semicircular pattern, with uniform spacing across different velocity levels. This result demonstrates the sensor's high sensitivity and uniform performance across various directions. Furthermore, the sensing points within a single flow direction exhibit good linearity and are well-aligned with the standard flow direction ($< 10°$ angular error), confirming the sensor's strong repeatability and acceptable accuracy in directional flow perception. However, slight discrepancies in the measured angles of attack remain, likely due to misalignment between the rotation axis of the waterproof housing and the true flow direction. Additional sources of error may include inconsistencies in adhesive thickness or minor distortions in cilia alignment during fabrication.

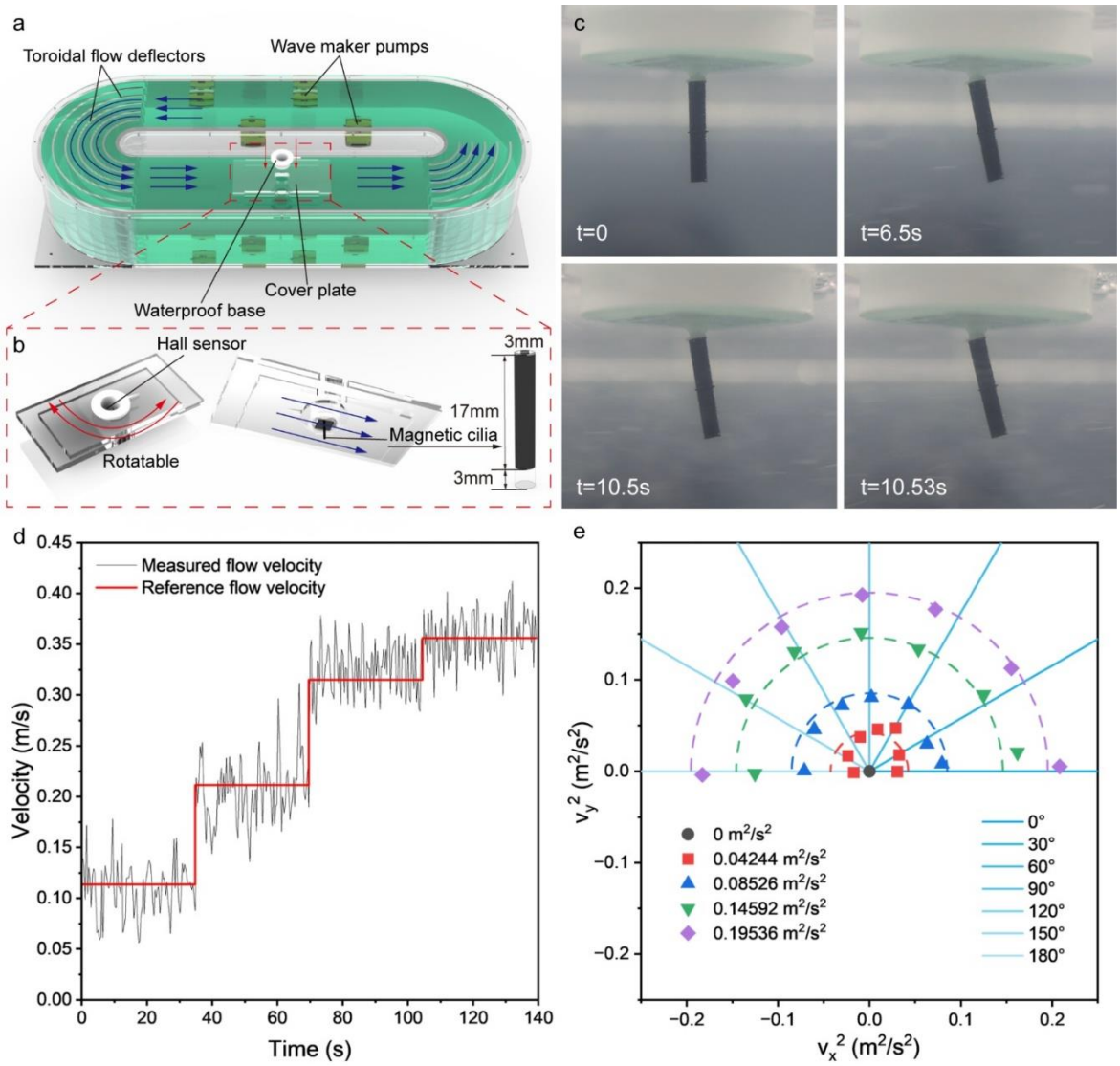

Fig. 5. (a) Experimental setup for generating a steady-state flow field. The dashed box indicates the region where the sensor is installed. (b) Schematic diagram of the sensor-based system for multidirectional flow field sensing. (c) Photograph showing the motion state of the magnetic cilium in the flow field experiment. (d) Comparison between flow velocities measured by the sensor and reference velocities. (e) Comparison between the squared flow velocities measured by the sensor at different angles and the corresponding reference velocities.

3.6 Experiments on Different Surfaces

As shown in Fig. 6(a), to evaluate the ability of the magnetic cilia to detect large-scale uneven surfaces, we allowed the cilia to sweep across an alternating concave-convex surface while recording the sensor outputs for further analysis. The results are shown in Fig. 6(b). By comparing these results with the actual surface features, the detection capability of the cilia on concave-convex surfaces can be assessed. We define an increase in the bending degree of the cilia as positive bending, and a decrease as negative bending. In the case of positive bending, the detected magnetic field deviates from the baseline, while during negative bending, it tends to return toward the baseline. As observed in Fig. 6(b), positive bending typically leads to a rapid rise followed by a drop in the measured magnetic field, which we refer to as the unstable region. This phenomenon arises because the surface constraints imposed on the cilia are displacement-based rather than force-based, as shown in Fig. 6(c). In contrast, negative bending often leads directly to a stable region due to the abrupt nature of the deformation, effectively skipping the unstable region. However, this unstable behavior can sometimes be captured—for instance, the sharp downward

spike near the 40-second mark in Fig. 6(b) indicates that a brief unstable region still exists during negative bending. The stable region also exhibits a slight upward drift in the direction of positive bending, attributed to the inelastic deformation of the cilia and the misalignment between the test surface and the sensor's reference plane. Overall, the measured results correspond well with the surface features and enable coarse quantitative analysis. For finer measurement precision, sensor arrays such as cilia arrays can be employed.

To further assess the sensor's capability in distinguishing surfaces of different materials, we performed additional tests by sweeping the magnetic cilia across four distinct textured surfaces. As shown in Fig. 6(e), from top to bottom visually, the materials were: foil knit, leather, felt fabric, and seersucker. The corresponding sensor outputs were recorded and analyzed, with high-pass filtering (MATLAB version R2023a, Fourth-order Butterworth filter) applied to remove the influence of surface waviness, as shown in Fig. 6(d). The results show noticeable differences in magnetic field responses across materials, which are directly related to the surface roughness of each material. These findings demonstrate the sensor's ability to discriminate between different surface types based on their texture. This accurate and reliable perceptual ability enables the sensor to tackle challenging tasks in versatile robotic systems, including but not limited to robotic arms, mobile robots, and healthcare devices.

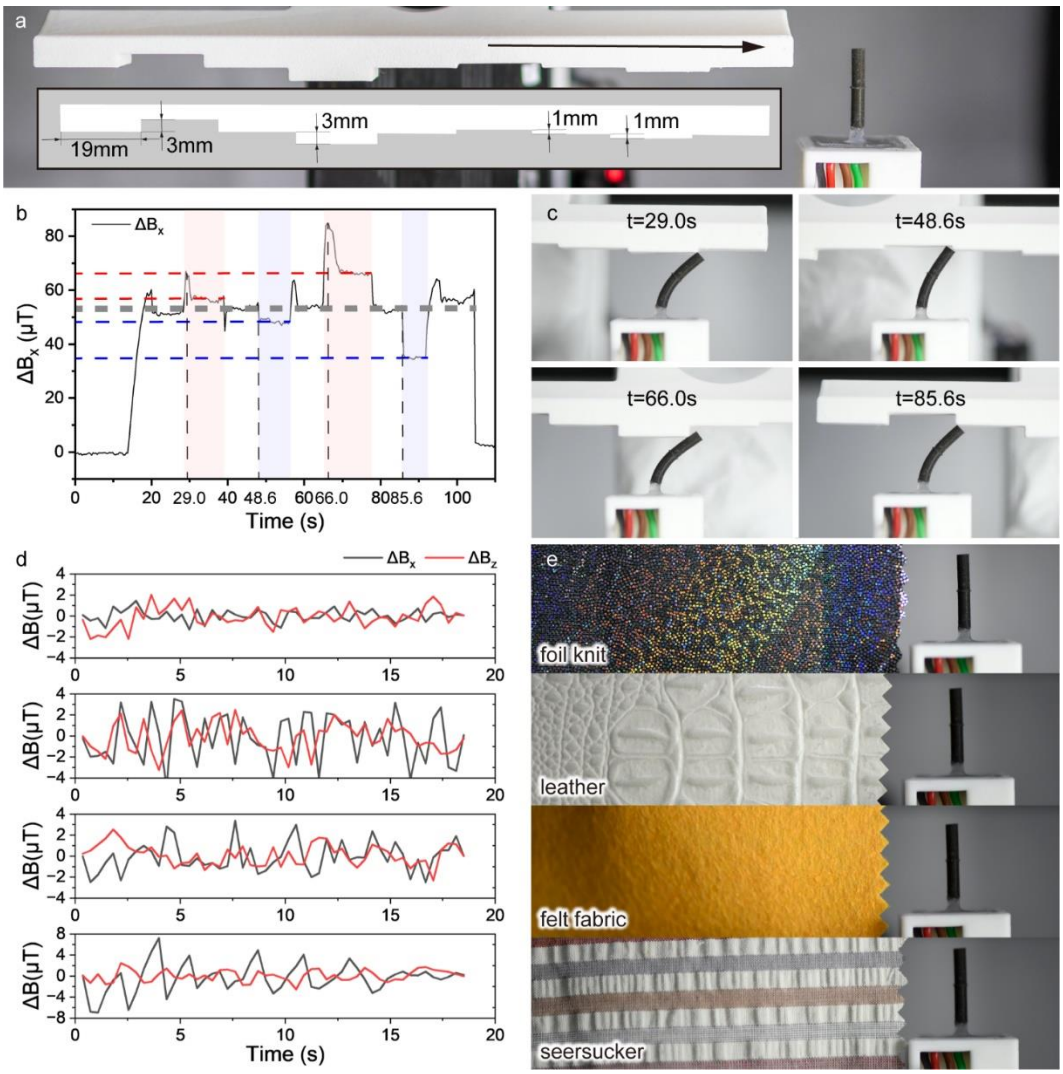

Fig. 6. (a) Overview of the experimental setup with the alternating concave-convex surface and magnetic cilia. (b) Magnetic field variations recorded as the cilia sweeps across the concave-convex surface. (c) Bending states of the cilia corresponding to key time points in (b). (d) Magnetic field variations measured while sweeping across surfaces of different materials, with high-pass filtering applied. (e) Photographs of the test surfaces with different textures; the total length of the magnetic cilia (20 mm) is shown for scale.

4 Conclusion

This study presents a theoretical and experimental framework for the design and optimization of biomimetic magnetic cilia-based tactile sensors, addressing the critical need for quantitative modeling in this emerging field. By integrating solid mechanics with magnetic dipole approximation, we developed a predictive model that accurately describes cilia deformation and the resulting magnetic field variations under both concentrated and distributed loading conditions. Experimental validation confirmed strong agreement between theoretical predictions and measured sensor responses ($R^2 > 0.99$ for field components), demonstrating the model's reliability in guiding sensor design.

The proposed approach overcomes the limitations of empirical trial-and-error methods, enabling systematic optimization of key parameters such as Young's moduli, aspect ratio, and magnetic segment proportion. This optimization led to enhanced sensitivity and performance in practical applications, including multidirectional flow field perception (0–0.5 m/s velocity range with high directional consistency), as well as surface profile recognition at both macroscopic (alternating concave-convex structures) and microscopic (material roughness) scales. The sensor's ability to resolve subtle variations in flow dynamics and surface topography highlights its potential for use in robotic manipulation, environmental monitoring, and human-machine interaction.

Beyond immediate applications, this work establishes a foundational methodology for future research in magnetic cilia-based sensing. The model's flexibility allows for adaptation to diverse sensing modalities, including pressure, shear, and vibration detection, while its scalability supports the development of high-density sensor arrays. Future efforts will focus on miniaturization, integration with flexible electronics, and exploration of advanced composite materials to further improve performance. Ultimately, this study advances robotic tactile perception by providing a physics-based design framework that bridges biomimetic inspiration with practical engineering implementation.

CRediT authorship contribution statement

Kan Liu: Conceptualization, Methodology, Validation, Resources, Data curation, Formal analysis, Visualization, Software, Writing – original draft, Writing – review & editing. Huangzhe Dai: Resources, Investigation. Kaicheng Luo: Methodology. Zuyao Zhang: Methodology. Chengfeng Pan: Investigation. Chengqian Zhang: Supervision, Conceptualization, Validation, Writing-review & editing. Peng Zhao: Funding acquisition, Supervision, Validation, Project administration, Writing – review & editing.

Declaration of Competing Interest

The authors declare that they have no known competing financial interests or personal relationships that could have appeared to influence the work reported in this paper.

Data Availability

Data will be made available on request.

Acknowledgements

This work was supported in part by the National Natural Science Foundation of China under grant 52205424; in part by the 2025 Chu Kochen College Deep Research Training Program under Grant 2025006; in part by the Zhejiang University Undergraduate Future Academic Rising Star Program; and in part by the National Postdoctoral Program for Innovative Talents under Grant BX20240321.

5 References

[1] X. Zhang, H. Hu, D. Tang, C. Zhang, J. Fu, P. Zhao, Magnetic flexible tactile sensor via direct ink writing, Sensors and Actuators A: Physical 327 (2021) 112753. https://doi.org/10.1016/j.sna.2021.112753.

[2] W. Xu, X. Li, R. Chen, W. Lin, D. Yuan, D. Geng, T. Luo, J. Zhang, L. Wu, W. Zhou, Ordered magnetic cilia array induced by the micro-cavity effect for the in situ adjustable pressure sensor, ACS Appl. Mater. Interfaces 14 (2022) 38291–38301. https://doi.org/10.1021/acsami.2c08124.

[3] Z. Zhang, Y. Wang, C. Zhang, W. Zhan, Q. Zhang, L. Xue, Z. Xu, N. Peng, Z. Jiang, Z. Ye, M. Liu, X. Zhang, Cilia-inspired magnetic flexible shear force sensors for tactile and fluid monitoring, ACS Appl. Mater. Interfaces 16 (2024) 50524–50533. https://doi.org/10.1021/acsami.4c12957.

[4] M. Ren, Q. Wu, Z. Yang, C. Jiang, X. Zhang, Z. Wang, Y. Guo, X. Huang, Flexible tactile sensors with self-assembled cilia based on magnetoelectric composites, ACS Appl. Mater. Interfaces 17 (2025) 6936–6947. https://doi.org/10.1021/acsami.4c18259.

[5] H. Ren, L. Yang, H. Chang, T. Zhang, G. Li, X. Yang, Y. Tang, W. Shang, Y. Shen, A robust and omnidirectional-sensitive electronic antenna for tactile-induced perception, Nat Commun 16 (2025) 3135. https://doi.org/10.1038/s41467-025-58403-3.

[6] J. Han, X. Dong, Z. Yin, S. Zhang, M. Li, Z. Zheng, M.C. Ugurlu, W. Jiang, H. Liu, M. Sitti, Actuation-enhanced multifunctional sensing and information recognition by magnetic artificial cilia arrays, Proceedings of the National Academy of Sciences 120 (2023) e2308301120. https://doi.org/10.1073/pnas.2308301120.

[7] J. Man, J. Zhang, G. Chen, N. Xue, J. Chen, A tactile and airflow motion sensor based on flexible double-layer magnetic cilia, Microsyst Nanoeng 9 (2023) 12. https://doi.org/10.1038/s41378-022-00478-9.

[8] H. Dai, C. Zhang, C. Pan, H. Hu, K. Ji, H. Sun, C. Lyu, D. Tang, T. Li, J. Fu, P. Zhao, Split-Type Magnetic Soft Tactile Sensor with 3D Force Decoupling, Adv. Mater. (2023) 2310145. https://doi.org/10.1002/adma.202310145.

[9] Y. Yan, Z. Hu, Z. Yang, W. Yuan, C. Song, J. Pan, Y. Shen, Soft magnetic skin for super-resolution tactile sensing with force self-decoupling, Sci. Robot. 6 (2021) eabc8801. https://doi.org/10.1126/scirobotics.abc8801.

[10] H. Dai, C. Zhang, H. Hu, Z. Hu, H. Sun, K. Liu, T. Li, J. Fu, P. Zhao, H. Yang, Biomimetic Hydrodynamic Sensor with Whisker Array Architecture and Multidirectional Perception Ability, Advanced Science 11 (2024) 2405276. https://doi.org/10.1002/advs.202405276.

[11] H. Hu, C. Zhang, X. Lai, H. Dai, C. Pan, H. Sun, D. Tang, Z. Hu, J. Fu, T. Li, P. Zhao, Large-area magnetic skin for multi-point and multi-scale tactile sensing with super-resolution, Npj Flex Electron 8 (2024) 1–12. https://doi.org/10.1038/s41528-024-00325-z.

[12] H. Hu, C. Zhang, C. Pan, H. Dai, H. Sun, Y. Pan, X. Lai, C. Lyu, D. Tang, J. Fu, P. Zhao, Wireless flexible magnetic tactile sensor with super-resolution in large-areas, ACS Nano 16 (2022) 19271–19280. https://doi.org/10.1021/acsnano.2c08664.

[13] T. Zhang, L. Jiang, H. Liu, Design and Functional Evaluation of a Dexterous Myoelectric Hand Prosthesis With Biomimetic Tactile Sensor, IEEE Trans. Neural Syst. Rehabil. Eng. 26 (2018) 1391–1399. https://doi.org/10.1109/TNSRE.2018.2844807.

[14] Q. Chen, R. Yang, D. Hu, Z. Ye, J. Lu, Artificial neurosynaptic device based on amorphous oxides for artificial neural network constructing, J. Mater. Chem. C 12 (2024) 9165–9174. https://doi.org/10.1039/D4TC01244E.

[15] J. Ge, X. Wang, M. Drack, O. Volkov, M. Liang, G.S. Cañón Bermúdez, R. Illing, C. Wang, S. Zhou, J. Fassbender, M. Kaltenbrunner, D. Makarov, A bimodal soft electronic skin for tactile and touchless interaction in real time, Nat Commun 10 (2019) 4405. https://doi.org/10.1038/s41467-019-12303-5.

[16] Z. Zhao, J. Tang, J. Yuan, Y. Li, Y. Dai, J. Yao, Q. Zhang, S. Ding, T. Li, R. Zhang, Y. Zheng, Z. Zhang, S. Qiu, Q. Li, B. Gao, N. Deng, H. Qian, F. Xing, Z. You, H. Wu, Large-scale integrated flexible tactile sensor array for sensitive smart robotic touch, ACS Nano 16 (2022) 16784–16795.

https://doi.org/10.1021/acsnano.2c06432.

[17] Y. Liu, H. Wo, S. Huang, Y. Huo, H. Xu, S. Zhan, M. Li, X. Zeng, H. Jin, L. Zhang, X. Wang, S. Dong, J. Luo, J.M. Kim, A flexible capacitive 3D tactile sensor with cross-shaped capacitor plate pair and composite structure dielectric, IEEE Sensors Journal 21 (2021) 1378–1385. https://doi.org/10.1109/JSEN.2020.3021010.

[18] B. Fang, Y. Chen, F. Sun, D. Yang, X. Zhang, Z. Xia, H. Liu, A petal-array capacitive tactile sensor with micro-pin for robotic fingertip sensing, in: 2020 3rd IEEE International Conference on Soft Robotics (RoboSoft), 2020: pp. 452–457. https://doi.org/10.1109/RoboSoft48309.2020.9116047.

[19] M.S. Ramasamy, R. Bhaskar, S.S. Han, Piezoelectric biosensors and nanomaterials-based therapeutics for coronavirus and other viruses: A mini-review, CTMC 23 (2023) 115–127. https://doi.org/10.2174/1568026623666221226091907.

[20] S. Park, G. Choi, M. Kang, W. Kim, J. Kim, H.E. Jeong, Bioinspired magnetic cilia: From materials to applications, Microsyst Nanoeng 9 (2023) 1–22. https://doi.org/10.1038/s41378-023-00611-2.

[21] J. Yu, M. Ai, C. Liu, H. Bi, X. Wu, W.B. Ying, Z. Yu, Cilia-inspired bionic tactile E-skin: Structure, fabrication and applications, Sensors 25 (2025) 76. https://doi.org/10.3390/s25010076.

[22] Y. Wan, Z. Qiu, Y. Hong, Y. Wang, J. Zhang, Q. Liu, Z. Wu, C.F. Guo, A highly sensitive flexible capacitive tactile sensor with sparse and high-aspect-ratio microstructures, Advanced Electronic Materials 4 (2018) 1700586. https://doi.org/10.1002/aelm.201700586.

[23] J. Man, Z. Jin, J. Chen, Magnetic tactile sensor with bionic hair array for sliding sensing and object recognition, Advanced Science 11 (2024) 2306832. https://doi.org/10.1002/advs.202306832.

[24] D. Sengupta, D. Trap, A.G.P. Kottapalli, Piezoresistive carbon nanofiber-based cilia-inspired flow sensor, Nanomaterials 10 (2020) 211. https://doi.org/10.3390/nano10020211.

[25] Z. Hu, C. Zhang, H. Sun, X. Ma, P. Zhao, Length manipulation of hard magnetic particle chains under rotating magnetic fields, Sensors and Actuators A: Physical 361 (2023) 114562. https://doi.org/10.1016/j.sna.2023.114562.

[26] H. Dai, Z. Wu, C. Meng, C. Zhang, P. Zhao, A magnet splicing method for constructing a three-dimensional self-decoupled magnetic tactile sensor, Magnetochemistry 10 (2024) 6. https://doi.org/10.3390/magnetochemistry10010006.

[27] J.C. Maxwell, A treatise on electricity and magnetism, Cambridge University Press, Cambridge, 2010. https://doi.org/10.1017/CBO9780511709340.